

HST and UKIRT imaging observations of $z \sim 1$ 6C radio galaxies - I. The data

K. J. Inskip¹*, P. N. Best², M. S. Longair¹, S. Rawlings³, H. J. A. Röttgering⁴ and S. Eales⁵

¹ Cavendish Laboratory, Madingley Road, Cambridge, CB3 0HE,

² Institute for Astronomy, Royal Observatory Edinburgh, Blackford Hill, Edinburgh, EH9 3HJ

³ Department of Astrophysics, University of Oxford, Keble Road, Oxford OX1 3RH

⁴ Sterrewacht Leiden, Postbus 9513, 2300 RA Leiden, the Netherlands

⁵ Department of Physics and Astrophysics, University of Wales Cardiff, PO Box 913, Cardiff CF2 3YB

arXiv:astro-ph/0308121v1 7 Aug 2003

ABSTRACT

The results of Hubble Space Telescope and UKIRT imaging observations are presented for a sample of 11 6C radio galaxies with redshifts $0.85 < z < 1.5$. The observations of the 6C sources reveal a variety of different features, similar to those observed around the higher power 3CR sources of similar redshifts. However, the extent and luminosity of the aligned emission appears less extreme in the case of the 6C radio galaxies. For both samples, the aligned emission clearly cannot be explained by a single emission mechanism; line emission and related nebular continuum emission, however, often provide a significant contribution to the aligned emission.

Key words: galaxies: active – galaxies: photometry – galaxies : evolution

1 INTRODUCTION

Powerful distant radio sources (up redshifts of at least unity) are usually hosted by giant elliptical galaxies. K -band observations of these galaxies show them to have de Vaucouleurs radial profiles, with the emission dominated by light from the old stellar populations (e.g. Best, Longair & Röttgering 1998). However, observations at shorter wavelengths frequently show the host galaxies to be surrounded by extensive regions of UV/optical continuum and line emission, particularly at redshifts $z > 0.3$. At higher redshifts ($z \gtrsim 0.6$) these regions of extended emission are usually observed to be closely aligned with the radio source axis (e.g. Chambers, Miley & van Breugel 1987; McCarthy et al 1987); this is known as the *Alignment Effect*.

Many different emission mechanisms have been proposed in order to account for the alignment effect; the most likely options include extended line emission and nebular continuum radiation (Dickson et al 1995), scattering of the UV continuum from the AGN (e.g. Tadhunter et al 1992; Cimatti et al 1993) and young stars produced in a radio jet induced starburst (McCarthy et al 1987). Generally, no single mechanism can account for all the excess emission forming the alignment effect. The relative contributions of each of these processes depend on several factors, including the available gas mass in the IGM, and the power of the radio source.

Additionally, the presence of shocks associated with the expanding radio source (evidence for which has been observed in the emission line spectra of many radio sources, e.g Clark et al 1998; Best, Röttgering & Longair 2000; Solózano-Iñarrea, Tadhunter & Axon 2001; Inskip et al 2002a) can also influence the continuum alignment effect. The passage of radio source shocks through the cool dense gas clouds can induce star formation (e.g. Dey et al 1997; Bicknell et al 2000). Ionizing photons associated with the shocks can boost the luminosity of certain emission lines, and cause increased nebular continuum emission. The passage of a fast shock can also potentially cause the break-up of optically thick clouds (Bremer, Fabian & Crawford 1997; Mellema, Kurk & Röttgering 2002), increasing the covering factor for scattering of the UV flux from the AGN. The more numerous, smaller clouds will also have a larger cross section for ionization by the AGN, leading to an increase in the total flux of line emission. However, although the presence of shocks can enhance the alignment effect, with the exception of jet-induced star formation shocks are not necessarily required.

Studies of 3CR radio galaxies (e.g. McCarthy, Spinrad & van Breugel 1995; Best, Longair & Röttgering 1997) have shown that the regions of extended optical/UV continuum emission surrounding the higher redshift sources in the sample are more extensive and better aligned with the radio source axis than for sources at lower redshifts. This may reflect a real evolutionary trend: changes in radio galaxy environment with cosmic epoch, particularly relating to the availability of cool dense gas clouds in the local IGM, could

* E-mail: kji@mrao.cam.ac.uk

clearly affect the observed alignment effect. However, the observed variation in the alignment effect with redshift for 3CR sources may instead be due to a number of selection effects, including the rest-frame wavelength of the observed emission, the size of the radio source and the radio source power. We now discuss each of these selection effects in turn.

(i) *Rest frame wavelength.* For observations at a given wavelength of a sample of galaxies covering a large redshift range, the rest-frame wavelength at which the galaxies are observed becomes longer at lower redshifts. As discussed above, at longer wavelengths the host galaxy dominates the light, and the alignment effect is weaker (Best, Longair & Röttgering 1997; Rigler et al 1992). Additionally, any wavelength dependence of the alignment effect will express itself as a change in observed aligned emission properties with redshift.

(ii) *Radio source size.* Radio galaxies at high redshift are observed to have typically smaller projected linear sizes than those nearby (e.g. Wardle & Miley 1974). In part, this is argued to be due to a selection bias within flux limited samples (e.g. Blundell, Rawlings & Willott 1999, Neeser et al 1995) caused by a combination of Malmquist bias and the decrease in radio luminosity with radio size for individual sources (Kaiser, Dennett-Thorpe & Alexander 1997). This change in mean size with redshift is potentially important, as many aligned emission properties show a strong variation with the size of the radio source. Best et al (1997) found that the emission surrounding the smaller radio galaxies in their sample was usually brighter and more extensive than that seen around the larger radio sources in the sample, and was better aligned with the radio axis, leading to an enhanced alignment effect. The effects of shocks are particularly pronounced in the case of smaller radio sources (i.e. those with a projected physical size of $< 120\text{kpc}$) and can lead to increased emission from the extended structures in these smaller sources. Therefore, at high redshifts, the larger number of radio sources with sizes comparable to the optical host galaxy sizes (or extended emission line region sizes) will increase the predominance of the alignment effect. However, this alone cannot account for the apparent redshift evolution of the alignment effect.

(iii) *Radio power.* One final problem with studies of flux limited samples of radio galaxies (such as the 3CR sample) is that the radio power of these sources increases with redshift, leading to a tight coupling between redshift and radio power. It is therefore unclear whether the observed variation in the alignment effect with redshift reflects a link between radio power and the strength of the observed alignment effect, or an evolutionary trend with cosmic epoch.

To improve our understanding of the relative contributions of different emission mechanisms to the alignment effect, the influence of radio power and redshift needs to be investigated independently. The 6C sample of radio galaxies (Eales 1985) provide a population of radio galaxies ideally suited for this investigation, as these galaxies are roughly a factor of 6 lower in radio power than 3CR sources at the same redshift. We have carried out a program of multiwavelength imaging and spectroscopic observations of a sub-sample of 11 6C radio sources at $z \sim 1$, which are well matched to the 3CR subsample previously studied by Best et al (1997, 1998, 2000). The results of these observations can then be contrasted with those of similar observations of 3CR sources matched in either redshift or radio power. By comparing Hubble Space Telescope (HST) and UKIRT observations of 6C and 3CR sources at $z \sim 1$, we can investigate the effect of radio power on the galaxy colours, and therefore the excess UV emission producing the alignment effect. These observations also allow us to study the morphologies of the

aligned structures surrounding distant radio galaxies at lower radio powers, and to determine whether radio power influences the extent and luminosity of the alignment effect, or the type of features observed.

The structure of the paper is as follows. In section 2, the sample selection, HST and UKIRT observations and the astrometry are outlined. In section 3 we present an analysis of the contribution of line and nebular continuum emission to the observed magnitudes. We present the HST and UKIRT images in section 4, and conclude with a discussion of the data in section 5. The full analyses of the properties of the host galaxy, the alignment effect and the galaxy colours, and the comparison of these results with a matched sample of 3CR galaxies at $z \sim 1$ are deferred to two subsequent papers in this series. Values for the cosmological parameters $\Omega_0 = 0.3$, $\Omega_\Lambda = 0.7$ and $H_0 = 65 \text{ km s}^{-1} \text{ Mpc}^{-1}$ are assumed throughout this paper.

2 SAMPLE SELECTION AND OBSERVATIONS

This paper focuses on observations of galaxies selected from the 6CER sample[†] (Rawlings, Eales & Lacy 2001), a revised version of the sample originally defined by Eales (1985). This revised sample is complete, and consists of 59 radio sources with flux densities at 151 MHz which fall in the range $2.0\text{Jy} < S_{151} < 3.93\text{Jy}$, and lie in the region of the sky $08^h20^m < \text{RA} < 13^h01^m$, $34^\circ < \text{Dec} < 40^\circ$. Eleven high redshift 6C sources within the redshift range $0.85 < z < 1.5$ have been selected from this sample, excluding those sources identified as quasars (Best et al 1999). Three further sources in this redshift range are not included in the sample. 6C1123+34 was excluded on the basis that it would be barely resolvable in the 5GHz radio observations of the sample. Additionally, the first estimate of the redshifts of 6C1212+38 and 6C1045+25 wrongly placed them outside the selection criteria for this sample. These galaxies were selected as a comparison sample matched in redshift to the 3CR $z \sim 1$ subsample of Best et al (1997). At these redshifts, 6C radio galaxies are approximately 6 times less powerful radio sources than 3CR galaxies.

2.1 HST observations

The Hubble Space Telescope (HST) observations were made in 1996/8 (6C0943+39, 6C1129+37, 6C1011+36, 6C1017+37, 6C1256+36) and 2000/1 (6C0825+34, 6C1019+39, 6C1100+35, 6C1204+35, 6C1257+36, 6C1217+36) under proposals #6684 and #8173 respectively. The instrument used for these observations was the Wide Field/Planetary Camera 2 (WFPC2). The dimensions of each of the WFPC2 chips are 800×800 pixels, and the scale of the three WF chips is $\sim 0.09953''$ per pixel, giving a total field of view of about $160 \times 160 \text{ arcsec}^2$. For the five sources observed in 1996/1998, the F702W filter was used. For the three high redshift sources ($z > 1.3$) observed in 2000/2001, observations were made using the F814W filter. These filters were chosen to be at the same rest-frame wavelength as the HST observations of the 3CR $z \sim 1$ sample of Best, Longair & Röttgering (1997). For the remaining three sources observed in 2000/2001, two filters were used (F606W and F814W). As well as covering the same rest-frame wavelength,

[†] Up-to-date information for the revised 6CE sample can be found at: <http://www-astro.physics.ox.ac.uk/~sr/6ce.html>.

the use of two filters provides colour information, which is particularly useful when studying the aligned emission. For the purposes of later clustering analysis, the target object was positioned towards the corner of the WF3 chip, at the approximate centre of the WF/PC field.

Observations in each filter consisted of 2-6 individual exposures of 1200s duration. All exposures were individually calibrated using the standard Space Telescope Science Institute (STScI) pipeline processing. After this stage, images made in the same filter for a given object were combined using the STSDAS IRAF package GCOMBINE. This package combines the data on each WFPC2 chip by weighted averaging, rejecting most ($\sim 95\%$) of the cosmic rays in the process. Any remaining cosmic rays were removed using the IRAF package COSMICRAYS, which rejects pixels above a threshold level on the basis of their flux ratio relative to the mean neighbouring pixel flux.

The WFPC2 CCDs have a small parallel charge transfer efficiency (CTE) problem. This correction for this was approximated by Holtzman *et al* (1995) as a linear function, whereby pixels values in row 1 remain unchanged, whilst the pixel values in row 800 need to be increased by a factor of 4%. Although a more realistic CTE estimate requires that the observing date, target pixel location, target counts and background level are also taken into account (Biretta, Lubin *et al* 2002, Dolphin *et al* 2000), for the setup of the current observations (high background levels, large aperture photometry) the Holtzman *et al* approximation (accurate to within 0.01 magnitudes) is fully consistent with the Dolphin *et al* corrections. Given that the error on this approximation is substantially smaller than the statistical photometric errors, the Holtzman *et al* correction was adopted for the sake of simplicity.

Photometry of the radio galaxies was carried out using the IRAF APPHOT packages. 9" diameter apertures were used in order to include most of the light from the host galaxy and aligned structures, and the background level was determined from an annulus surrounding the object aperture. The background level statistics were also measured for 30 apertures in empty regions of the sky, in order to estimate the systematic uncertainty of the background subtraction due to variations in sky intensity across the field of view. For some sources, flux from neighbouring objects lay within the 9" object apertures. Where the objects were well separated from the radio galaxy, the additional flux could be estimated and was removed from the aperture counts. For later analysis of the colours of the target objects, flux was also measured in a 4" diameter aperture. In this case, any flux contamination by other objects was generally negligible, and no corrections were necessary.

WFPC2 counts were converted to photometric magnitudes using the method described by Holtzman *et al* (1995):

$$m = -2.5 \log_{10} \left(\frac{F}{T \times 1.1 \times 2.006} \right) + M_{ZP}$$

where F is the measured object counts, T is the exposure time and M_{ZP} is the zero point magnitude for the filter. The zero point magnitudes used are the most recent update[†] based on the data presented in Dolphin (2000); these are 22.101, 21.674 and 20.855 for the F606W, F702W and F814W filters respectively. The factor of 2.006 corresponds to the required gain conversion for the WF3 chip, since the photometric calibration data for WFPC2 are observed with a gain of $14e^-/DN$, whereas these observations were made with a gain of $7e^-/DN$. The additional factor of 1.1 is required to account for aperture correction of observations

[†] see http://www.noao.edu/staff/dolphin/wfpc2_calib/

of photometric standard stars (Holtzman *et al* 1995). The resulting magnitudes have been corrected for galactic extinction using the $E(B - V)$ for the Milky Way from the NASA Extragalactic Database (NED) and the parametrized galactic extinction law of Howarth (1983).

There are several sources of uncertainty in the measurement of HST fluxes. Errors in the photometric calibration include 1% for the CTE effect, 1% for the gain ratio correction, 1% for the photometric aperture corrections and 2% from the accuracy of the zero point magnitudes. Added in quadrature to these are the photometry errors determined using APPHOT: the percentage error due to the Poisson noise from the detected counts ($1/\sqrt{G \times N_f \times C}$, where G is the Gain, N_f is the number of frames used in each GCOMBINED exposure, and C is the total counts per frame in the aperture), the percentage random error due to the sky counts in the aperture ($(\sqrt{N_{pix}} \times \sigma)/C$, where N_{pix} is the number of pixels in the object aperture, and σ is the mean standard deviation of the sky counts, calculated from 30 different sky apertures), and the percentage error due to the accuracy to which the mean sky value can be calculated ($(N_{pix} \times E_{Sky})/C$). For this last systematic source of error, the sky error E_{Sky} is calculated as the standard deviation of the 30 mean sky values calculated in apertures at different locations on the CCD. These errors differ slightly from the APPHOT values for a single sky aperture, due to the additional consideration of systematic errors in the sky subtraction.

All magnitudes quoted in this paper for the HST observations use HST filters. Conversions to ground based *UBVRI* magnitudes can be determined using the tabulated filter data in Holtzman *et al* (1995), although this would add large uncertainties to the galaxy colours. For a rough comparison with ground based magnitudes, $F814W \approx I + 0.07(V - I)$, $F702W \approx R - 0.3(V - R)$ and $F606W \approx V - 0.25(V - I)$. Full details of the HST observations are displayed in Table 1.

2.2 UKIRT observations

The majority of the UKIRT observations were carried out over four nights in March 2001 using UFTI (the UKIRT Fast-Track Imager). This is a 1–2.5 μ m camera with a 1024×1024 HgCdTe array and a plate scale of 0.091" per pixel, which gives a field of view of 92". These observations were made in the *J*, *H* and *K* infrared wavebands for each source; full observational details are tabulated in Table 2. The *K*-band observations were generally of 1-2 hours duration in total. *J*-band observations were typically 18-45 minutes, and *H*-band observations typically 9-18 minutes.

Service time observations were also taken in order to make up for time lost due to poor weather. Of these observations, the *H*-band service observations of 6C1204+35, 6C1217+36 and 6C1257+36 were carried out using IRCAM3. IRCAM3 is a cooled 1–5 μ m camera with a 256×256 InSb array and a plate scale of 0.081" per pixel, which gives a field of view of 20.8". Additional UFTI observations of 6C1100+35, 6C1129+37 and 6C1204+35 were kindly obtained in April 2002 by Mairi Brookes and Philip Best.

All observations used a nine point jitter pattern, with offsets of roughly 10" between each 1 minute exposure (with the exception of the IRCAM3 service observations, which used only 4 pointings per jitter pattern). The observational data were dark subtracted, and masked for bad pixels. Blocks of up to 120 frames of data were combined and median filtered to create a first-pass sky flat-field image, which accounted for the majority of the pixel-to-pixel variations of the chip. However, large-scale illumination gradients

Table 1. Full details for the HST observations. The dates of observations are given in column 3; those made in 1996/8 were under proposal #6684, and those in 2000/1 under proposal #8173. The filter details are given in columns 4 and 5, and the exposure times of the observations are listed in column 6. Columns 7 and 8 give the photometric magnitudes and errors determined in a 9'' diameter aperture. These 9'' magnitudes have been corrected for flux contamination by adjacent objects. 4'' diameter aperture magnitudes and their associated errors are given in columns 9 and 10. The 4'' magnitudes do not include any correction for flux contamination by nearby objects. All magnitudes have been corrected for galactic extinction.

[1] Source	[2] z	[3] Observation Date	[4] Filter	[5] Central Wavelength [Å]	[6] Exposure Time [s]	[7] 9'' WFPC Magnitude	[8] Error	[9] 4'' WFPC Magnitude	[10] Error
6C0825+34	1.467	17/03/00	F814W	7924	7200	21.65	0.15	22.10	0.17
6C0943+39	1.035	19/05/96	F702W	6862	4800	21.78	0.38	22.08	0.14
6C1011+36	1.042	19/03/98	F702W	6862	4800	21.59	0.19	21.73	0.07
6C1017+37	1.053	14/05/98	F702W	6862	4800	21.53	0.16	21.77	0.06
6C1019+39	0.922	14/05/00	F606W	5934	2400	21.89	0.25	22.01	0.08
			F814W	7924	2400	19.86	0.10	20.07	0.04
6C1100+35	1.440	17/05/00	F814W	7924	7200	21.80	0.18	21.80	0.06
6C1129+37	1.060	08/05/96	F702W	6862	4800	21.52	0.14	22.02	0.07
6C1204+35	1.376	11/05/00	F814W	7924	7200	20.79	0.29	21.30	0.10
6C1217+36	1.088	15/04/01	F606W	5934	2400	22.26	0.32	22.25	0.09
			F814W	7924	2400	20.59	0.12	20.89	0.05
6C1256+36	1.128	05/07/98	F702W	6862	4800	22.23	0.16	22.66	0.09
6C1257+36	1.004	01/07/00	F606W	5934	2400	22.04	0.26	22.48	0.09
			F814W	7924	2400	20.55	0.12	20.98	0.05

remained, due to the changing position of the telescope over the night. To correct for this, smaller groups of 9 – 18 first pass flat-fielded images were similarly combined to create residual sky flat-field images, which successfully accounted for this effect. Bright objects on the flat-fielded images were then masked out, and the process repeated, allowing the data to be cleanly flat fielded without any contamination from stars or galaxies.

The flat-fielded data for each source were sky-subtracted and combined using the IRAF package DIMSUM, creating a final mosaiced image of approximately 115×115 arcsec 2 [§], which was flux calibrated using observations of UKIRT faint standard stars. Photometry was carried out within 9'' and 4'' diameter apertures using the IRAF package APPHOT and a single sky annulus, correcting for the presence of companion objects in the larger 9'' apertures only. Galactic extinction corrections and uncertainties for the resulting magnitudes were determined in the same way as for the HST observations. The resulting magnitudes presented in Table 2 are generally in very good agreement with previous *K* band photometry of these galaxies (Lilly, Longair & Allington-Smith 1985; Eales et al 1997).

2.3 Astrometry

Astrometric solutions for the pixel scales and rotations of the HST and UKIRT images were determined using the method outlined below. Firstly, the pixel position of unsaturated stars present in both the image and in the APM database (Maddox *et al* 1990) were registered. As the 6C sources were selected at a significant distance from the plane of the Milky Way, a sufficient number of APM stars were not always available in the field of view of the observations. Where an inadequate number of unsaturated stars were available, compact elliptical galaxies with APM positions were also used if practical. The data were used to calculate an accurate measure of the pixel scales and the angle of rotation of the coordinate system.

[§] The highest signal-to-noise level is restricted to the central 70×70 arcsec 2 .

This first method worked fairly well for the majority of the sources. For a few sources however, no reasonable fits were achievable due to a lack of sufficient APM stars. In these cases, the UKIRT pixel scale and rotation were fixed at the mean of the values determined in other observations (these are stable at $< 1^\circ$) and the position of bright objects measured from the digitised sky survey was used to fit the right ascension and declination of the image. Comparison of the pixel positions of the numerous APM unidentified objects common to both the UKIRT and HST images then allows accurate determination of the HST astrometry.

Using both these methods where necessary, the astrometric errors are estimated to be less than about 0.5'', and usually better than 0.25''. The HST and UKIRT images of each source were spatially aligned to an accuracy of better than 0.1''.

3 CONTRIBUTION OF LINE EMISSION AND NEBULAR CONTINUUM EMISSION TO THE HST MAGNITUDES

3.1 Percentage contribution of line emission to the HST magnitudes

Due to the fact that for each source, several prominent emission lines lie within the wavelength range of the HST filters, it is important to estimate the contribution of line emission to the HST magnitudes. The emission line contribution was derived from spectroscopic observations of each source, assuming that the distributions of line and continuum emission were comparable, and so the equivalent widths of the emission lines in the spectral slit region were comparable to those in the entire source. For the eight sources with $z < 1.2$ the deep spectroscopic observations of Inskip *et al* (2002a) were used. For the remaining three higher redshift sources, the shallower Rawlings *et al* (2001) spectra were used. The results of this analysis are tabulated in Table 3.

The line emission contribution to the total UV excess varies from 3–18%, and as expected is less on average for the 6C sources than for the more powerful 3CR radio sources observed by Best *et al* (1997) at the same redshift. However, due to the lower radio power of the 6C sample, and the evidence that emission line flux

Table 2. Full details of UKIRT observations for the eleven 6C sources. The dates of observations are given in column 4. An ^S indicates that the observations were made in service mode, ^B indicates data were taken by Mairi Brookes and Philip Best, and ^I denotes that the observations used IRCAM3 rather than UFTI. Column 5 lists the seeing conditions of each set of observations, and column 6 gives the total useful exposure time in seconds, with the total photometric exposure time in brackets. 9'' diameter aperture *J*, *H* and *K* magnitudes are given in column 7 with their associated error (column 8). 4'' diameter aperture *J*, *H* and *K* magnitudes are given with their associated error in columns 9 and 10. For the 9'' magnitudes only, corrections have been made for flux contamination from adjacent objects. All magnitudes have been corrected for galactic extinction.

[1] Source	[2] z	[3] Filter	[4] Observation Dates	[5] Seeing (arcsec)	[6] Exposure Time [s]	[7] 9'' aperture Mag.	[8] Error	[9] 4'' aperture Mag.	[10] Error
6C0825+34	1.467	J	05/03/01	0.7	1080 (1080)	19.27	0.27	19.86	0.17
		H	07/03/01, 16/02/02 ^S	1.2, 0.7	1080 (540)	18.99	0.48	19.68	0.29
		K	04/03/01, 06/03/01, 07/03/01	1.3, 1.1, 1.1	9240 (4200)	18.90	0.24	19.12	0.12
6C0943+39	1.035	J	04/03/01	0.9	2700 (2700)	19.14	0.12	19.70	0.12
		H	06/03/01	0.8	1080 (1080)	18.64	0.17	19.27	0.14
		K	04/03/01, 05/03/01, 06/03/01	0.9, 0.8, 1.0	5760 (3660)	18.03	0.11	18.09	0.07
6C1011+36	1.042	J	05/03/01	0.7	1080 (1080)	19.59	0.28	19.68	0.20
		H	06/03/01	0.8	540 (540)	18.60	0.24	18.63	0.10
		K	05/03/01, 06/03/01	0.6, 0.9	4320 (3900)	17.67	0.09	17.83	0.06
6C1017+37	1.053	J	05/03/01	0.6	960 (960)	19.35	0.20	19.89	0.16
		H	06/03/01, 06/02/02 ^S	0.8, 0.6	3820 (3820)	18.98	0.19	19.54	0.15
		K	05/03/01, 06/03/01, 07/03/01	0.6, 0.7, 1.2	5700 (3480)	18.31	0.08	18.57	0.09
6C1019+39	0.922	J	04/03/01	0.8	1620 (1620)	18.00	0.06	18.47	0.07
		H	06/03/01	0.8	480 (480)	17.37	0.09	17.71	0.06
		K	04/03/01, 06/03/01	0.7, 0.7	4140 (2160)	16.41	0.04	16.80	0.04
6C1100+35	1.440	J	05/03/01, 25/04/02 ^B	0.7, 0.7	1620 (1620)	19.45	0.19	19.59	0.12
		H	06/03/01	0.7	1080 (1080)	18.70	0.19	19.02	0.11
		K	05/03/01, 06/03/01, 26/04/02 ^B	0.8, 0.7, 0.4	6960 (5340)	18.19	0.12	17.99	0.07
6C1129+37	1.060	J	05/03/01, 25/04/02 ^B	0.9, 0.7	2160 (2160)	19.38	0.20	19.35	0.11
		H	06/03/01	0.7	480 (480)	18.24	0.23	18.31	0.09
		K	04/03/01, 06/03/01, 24/04/02 ^B	1.0, 0.7, 0.8	6240 (1620)	17.63	0.11	17.81	0.07
6C1204+35	1.376	J	05/03/01, 25/04/02 ^B	0.9, 0.7	2160 (2160)	18.73	0.10	19.31	0.11
		H	14/04/01 ^{S,I}	0.6	720 (720)	18.59	0.26	18.76	0.11
		K	05/03/01, 06/03/01, 07/03/01, 22/04/02 ^B	1.0, 0.6, 0.9, 0.4	7500 (6900)	17.85	0.08	18.01	0.07
6C1217+36	1.088	J	04/03/01	1.2	1560 (1560)	19.26	0.16	19.50	0.12
		H	14/04/01 ^{S,I}	0.6	1440 (1440)	17.95	0.13	18.51	0.07
		K	04/03/01, 06/03/01, 07/03/01	0.8, 0.6, 0.9	6960 (1140)	17.22	0.08	17.55	0.06
6C1256+36	1.128	J	04/03/01	1.2	1440 (1440)	19.11	0.16	19.74	0.20
		H	07/03/01	0.6	540 (540)	18.11	0.14	18.58	0.09
		K	04/03/01, 06/03/01, 07/03/01	0.8, 0.8, 0.7	7800 (4620)	17.45	0.07	17.83	0.06
6C1257+36	1.004	J	05/03/01	1.0	1080 (1080)	19.15	0.17	19.39	0.11
		H	14/04/01 ^{S,I}	0.6	720 (720)	18.04	0.17	18.27	0.07
		K	05/03/01, 06/03/01, 07/03/01	1.0, 0.7, 0.6	7260 (5760)	17.17	0.05	17.50	0.05

scales with radio power (e.g. Inskip *et al* 2002a, Jarvis *et al* 2001), one might expect line emission to account for an even lower fraction of the total optical/UV excess observed in the 6C observations than is actually observed. However, the choice of filters is such that the wavelength of the dominant [OII] emission line is at a higher filter throughput for the 6C observations than the 3CR observations. As this is the most prominent emission line in the spectra of these galaxies at the wavelengths in question, the emission line contribution initially appears to be higher than might be expected for the 6C sources.

3.2 Spatial variation of emission line contribution

As fairly large emission line contributions are measured for several sources, it is well worth estimating how these emission lines contribute to the extended aligned emission. This can only be effectively done for the sources with emission line regions extended on scales significantly larger than the seeing, for which good 2-d spectra are available, i.e. 6C0943+39 and 6C1129+37. Although

6C1017+37 also has a strong emission line contribution, this source is not considered as it is not particularly extended in either the spectra or in the HST image.

For both sources, the HST image was convolved with a Gaussian in order to approximate the 1.5'' ground-based seeing conditions of the spectra. Then, the amount of flux in the HST image which would fall within the 2'' wide slit used for our spectroscopic observations was obtained. This was separated into three regions: a central 4'' region centred on the radio galaxy, and two regions either side, from 2'' out to 4.5'' from the centre of the galaxy (this corresponds to the limiting extent of the 9'' diameter apertures used in the photometry). Next, the 2-d surface brightness profile of the [OII] emission line (Inskip *et al* 2002a) was used to determine the emission line flux for the central 4'', and the regions outside. These values were used to determine how the ratio of emission line flux to total flux varied in the central, east and west regions.

For 6C0943+39, the HST flux falling in the central region of the slit was found to be 17.5% line emission. The outer regions were found to be similar on either side of the galaxy; here emission

Table 3. Contributions of line emission and continuum emission to the HST magnitudes. The fifth column lists the emission lines which lie within the spectral range of the observations, and the sixth the percentage of the total magnitude which can be accounted for by line emission, plus the associated error. The seventh column gives the percentage of the total flux in each filter which can be accounted for by nebular continuum emission and the associated error. Where only an upper limit is available for the $H\beta$ flux, the nebular continuum percentage is denoted as an upper limit.

[1] Source	[2] Filter	[3] 9'' WFPC Mag.	[4] Error	[5] Emission Lines	[6] Line Emission Flux	[7] Nebular Continuum Flux	[7] Error
6C0825+34	F814W	21.65	0.15	[NeV],[OII],[NeIII],H ζ ,[NeIII]+He	3%	$\pm 2\%$	< 16% $\pm 3\%$
6C0943+39	F702W	21.78	0.38	[NeV],[OII],[NeIII],[NeIII]+He	18%	$\pm 5\%$	< 6% $\pm 1\%$
6C1011+36	F702W	21.59	0.19	[NeV],[OII],[NeIII],H ζ ,[NeIII]+He,H δ	8%	$\pm 4\%$	16% $\pm 5\%$
6C1017+37	F702W	21.53	0.16	[NeV],[OII],[NeIII],H ζ ,[NeIII]+He,H δ	17%	$\pm 4\%$	25% $\pm 6\%$
6C1019+39	F606W	21.89	0.25	[NeV],[OII]	3%	$\pm 2\%$	< 3% –
	F814W	19.86	0.10	[OII],[NeIII],H β	5%	$\pm 1\%$	< 0.5% –
6C1100+35	F814W	21.80	0.18	[NeV],[OII],[NeIII],H ζ ,[NeIII]+He,H δ	7%	$\pm 4\%$	< 1% $\pm 0\%$
6C1129+37	F702W	21.52	0.14	[NeV],[OII],[NeIII],[NeIII]+He	15%	$\pm 5\%$	< 22% $\pm 3\%$
6C1204+35	F814W	20.79	0.29	[NeV],[OII],[NeIII],H ζ ,[NeIII]+He,H δ	11%	$\pm 7\%$	< 31% $\pm 4\%$
6C1217+36	F606W	22.26	0.32	CII],[NeIV],[NeV]	0%	$\pm 1\%$	< 1% –
	F814W	20.59	0.12	[NeV],[OII],[NeIII],H γ	3%	$\pm 1\%$	< 1% –
6C1256+36	F702W	22.23	0.16	[NeV],[OII],[NeIII],H ζ	9%	$\pm 4\%$	33% $\pm 10\%$
6C1257+36	F606W	22.04	0.26	CII],[NeIV],[NeV]	2%	$\pm 1\%$	27% $\pm 10\%$
	F814W	20.55	0.12	[OII],[NeIII],H ζ ,[NeIII]+He,H γ ,H β	10%	$\pm 2\%$	25% $\pm 13\%$

lines account for 39.5% of the total flux (c.f. 18% line emission in total). 88% of the total emission lies within the central region, whereas 91% of the total continuum emission and 77% of the total line emission lie within this region. For this source, the extended faint emission includes a stronger contribution from line emission.

For 6C1129+37, the HST flux falling in the central region of the slit was found to be 20% line emission. The flux in the 2.5'' region of the slit to the west of the host galaxy was found to be 7.8% line emission, the flux in the east region is 13.4% line emission (c.f. 15% line emission in total). Clearly, for this source, emission lines do not dominate the more extended regions of emission.

3.3 Nebular continuum emission

Emission lines clearly provide a significant fraction of the flux observed in the HST images. In addition to line emission, nebular continuum radiation is also produced due to other radiative processes associated with the ionized gas. (These include free–bound (recombination) and free–free (bremsstrahlung) transitions involving hydrogen and helium, and the two–photon decay of the 2^2S level of hydrogen.) It is likely that nebular continuum emission will be an important factor for some sources. The level of the nebular continuum emission can be defined as a function of wavelength (in Angstroms) as:

$$F_\nu(neb) = \frac{3 \times 10^{-22} F(H\beta) \gamma_{tot}(\lambda)}{(1+z) \lambda^2 B}$$

where $\gamma_{tot}(\lambda)$ is the total emission coefficient for the different physical processes which cause the nebular continuum emission, $F(H\beta)$ is the $H\beta$ flux and B is a constant (1.24×10^{25} for an assumed temperature of 10^4 K). Values for these parameters have been taken from Aller *et al* (1987). This method for calculating the nebular continuum level is also the same as that used by Dickson *et al* (1995). $H\beta$ fluxes are the same as those used by Inskip *et al* (2002b) for the sources at $z < 1.2$. For the higher redshift 6C sources an upper limit on $H\beta$ has been calculated from the average line ratios tabulated in Inskip *et al* (2002a) and the emission line fluxes of Rawlings *et al* (2001).

The contribution of the nebular continuum to the total flux in each filter has been calculated using the formula above, and the re-

sults listed in Table 3. The derived percentages typically vary by $< 3\%$ if alternative temperatures of 5000 or 20000K are assumed instead; this has been added in quadrature with the $H\beta$ flux uncertainty to give the error values in column 7. For the sample as a whole, the nebular continuum contributions range from 0% to 33% of the total flux. This range is comparable to the 3% to 40% contribution of nebular continuum emission to the total UV continuum flux found by Tadhunter *et al* (2002) for a complete, unbiased sample of $0.15 < z < 0.7$ 2-Jy radio galaxies.

For 6C0943+39 and 6C1129+37, the nebular continuum contribution can also be estimated as a function of position. The percentage contribution of nebular continuum emission is 6% for the central regions of 6C0943+39, rising to 13% outside the central 4''. For 6C1129+37, nebular continuum emission contributes 29% of the total flux in the central region, 11% in the west region and 20% in the east region.

4 MULTI-WAVELENGTH IMAGES OF THE 6C $z \sim 1$ SUBSAMPLE

In this section the images of the galaxies in the optical, infrared and radio wavebands are presented (Figs. 1–11). The HST and UKIRT K -band images have been overlaid with 5GHz Very Large Array (VLA) radio contours. Zoomed-in images of the host galaxy are also provided for the larger radio sources in the sample. For the two sources which seem to have very close companion galaxies (6C1129+37 and 6C1256+36), close-ups of the HST images with UKIRT K -band contours are also presented.

The eleven sources are presented in order of increasing right ascension. All coordinates are in equinox J2000.0. A brief description of the key features of each source is also provided.

6C0825+34

6C0825+34, at $z = 1.46$, is the faintest and most distant galaxy in the sample. The UKIRT K -band image (Fig. 1) shows an approximately elliptical host galaxy. A faint tail of aligned emission

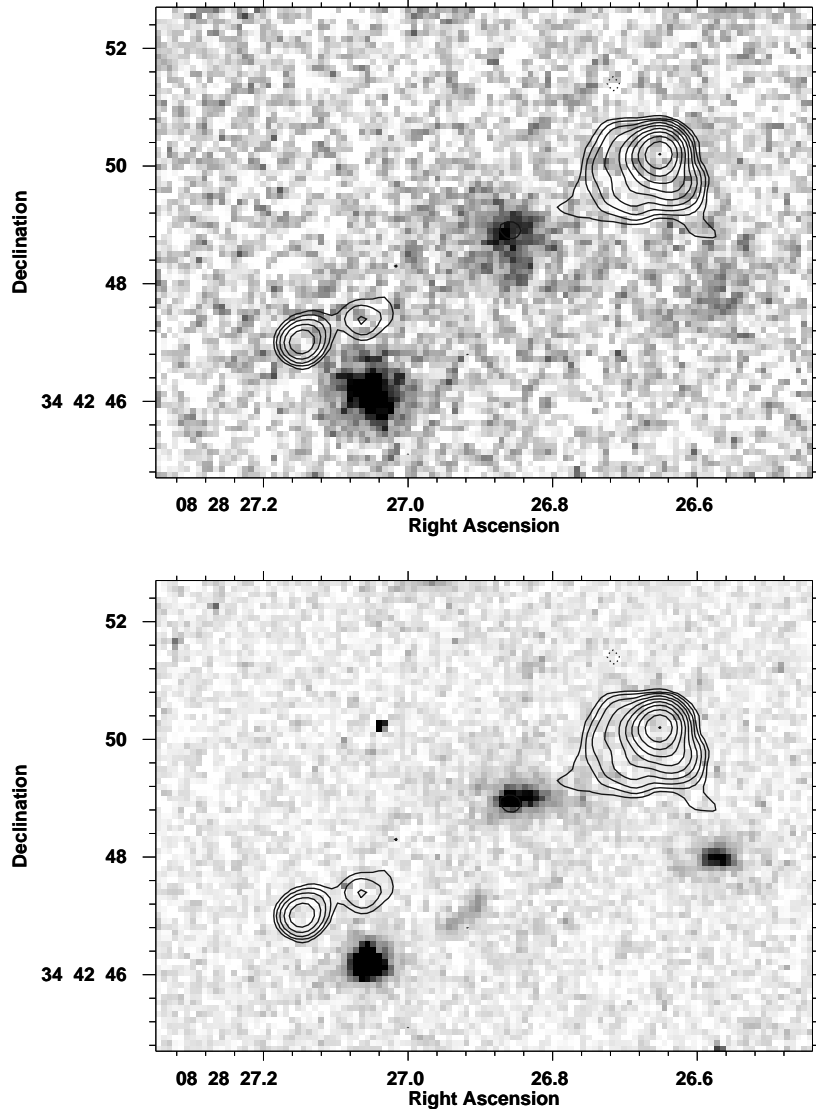


Figure 1. 6C0825+34: (a - top) K -band image of 6C0825+34. (b - bottom) HST F814W image of 6C0825+34. Contour lines for both images represent the 5GHz VLA observation of this source, with contours at $100\mu\text{Jy beam}^{-1} \times (-1, 1, 2, 4, \dots, 1024)$. All coordinates are in epoch J2000.0.

can be seen on the HST F814W image. 6C0825+34 has much bluer $J - K$ and $H - K$ colours than the other galaxies in the sample. Its F814W- K colour is average for the 6C sample, but low when compared to other 6C or 3CR sources at similar redshifts. The very blue colour of this source could be explained by some contamination from an incompletely obscured AGN. The deep VLA radio observations made of this source are also interesting (Best *et al* 1999) in terms of interpreting the observed colours. The north west radio lobe displays little depolarization at 5GHz, whereas the south east lobe is completely depolarized. Whilst this strong asymmetry in the flux levels of the radio lobes would favour a radio axis at a relatively large angle to the plane of the sky, the lack of a strong radio core argues against this interpretation. Additionally, the radial profile of the HST emission (see Paper 2 for the full analysis of the radial profiles) shows no evidence for a point source component, suggesting that a different interpretation is required for the very blue F814W- K colour of this source.

6C0943+39

6C0943+39, at $z = 1.036$, is clearly shown to be a bright elliptical galaxy in the K -band (Fig. 2). The colours of this source are average for the sample. The HST image shows extensive faint aligned emission surrounding the elliptical host galaxy. The more extended features include a strong contribution from line emission and nebular continuum emission ($\sim 50\%$ in total; see Section 3). At a distance of roughly $5''$ to the east of the elliptical host galaxy (outside the $9''$ diameter aperture used for the photometry), three bright emission regions can be seen, which may possibly be associated with the radio source. These appear to lie within the radio lobe, and form a line roughly perpendicular to the radio axis. Line emission is also observed in this region, with a narrower line width than is seen closer to the host galaxy. The colours of these three features are relatively blue in comparison with the radio galaxy itself.

With a projected angular size of 90kpc , 6C0943+39 is one of the smaller radio sources in the subsample. A faint radio core is observed at 5GHz, coincident with the elliptical host galaxy. The radio observations (Best *et al* 1999) also show that the eastern lobe

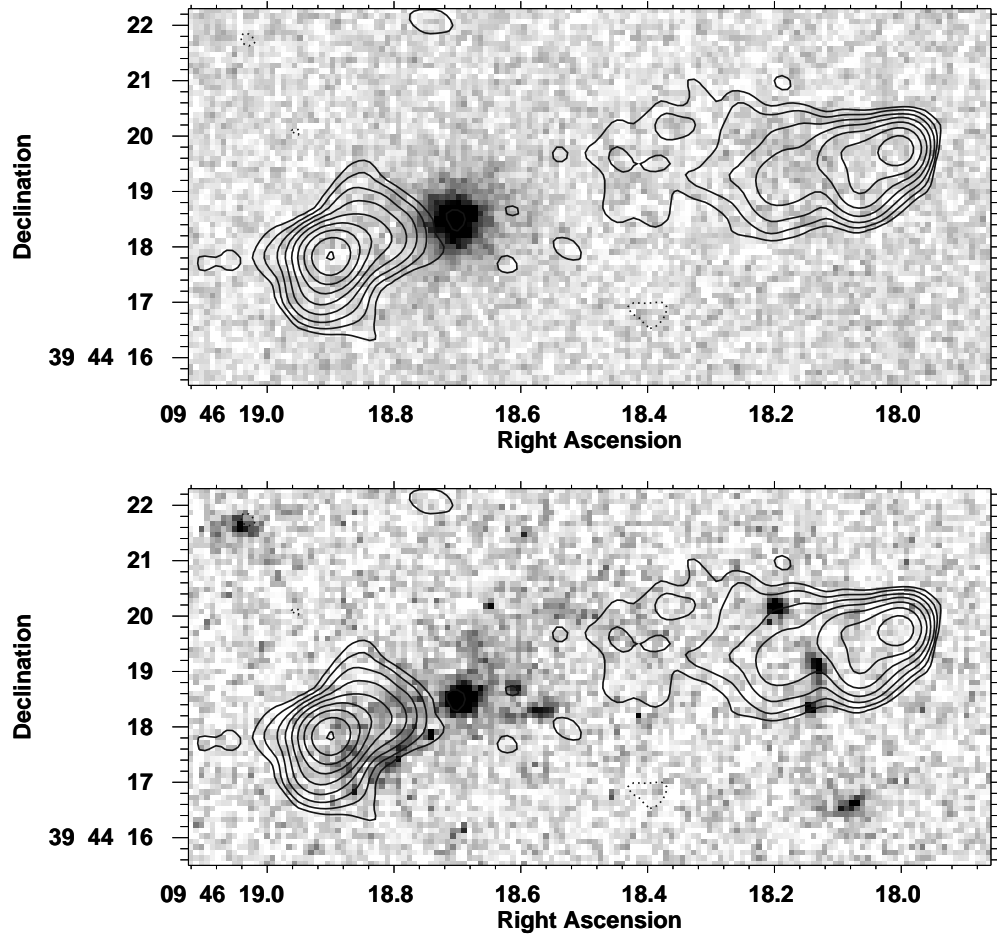


Figure 2. 6C0943+39: (a - top) *K*-band image of 6C0943+39. (b - bottom) HST F702W image of 6C0943+39. Contour lines for both images represent the 5GHz VLA observation of this source, with contours at $90\mu\text{Jy beam}^{-1} \times (-1, 1, 2, 4, \dots, 1024)$. All coordinates are in epoch J2000.0.

is strongly depolarized, and that there may be a sharp bend in the radio emission near the hotspot.

The spectroscopic observations of this source are consistent with shocks as the major ionization mechanism, which may perhaps account for the greater importance of line emission in the extended features surrounding this galaxy (Inskip et al 2002a). The odd L-shaped two dimensional profile of the [OII] 3727 emission line for this source may reflect the morphology of the aligned structures seen in the HST observations: the broader line emission may be associated with the diffuse UV emission aligned with the radio axis in the central 4'' region, and the less extreme gas kinematics may perhaps be linked to the bright knotty features to the west of the host galaxy.

6C1011+36

6C1011+36, at $z = 1.042$, is the largest radio source in the sample with a projected size of 444 kpc. The relative contribution of the core flux density to the total flux density is high, and a double hotspot is observed in the southern radio lobe. The HST image (Fig. 3) shows the elliptical host galaxy and a very bright blue feature towards the north west, loosely aligned with the radio source axis. This feature is not observed in the *K*-band observations of 6C1011+36. Due to its proximity to the host galaxy it is difficult to separate the flux due to this feature from that of the host

galaxy itself. However, an analysis of the flux in a small 0.6'' diameter aperture centred on this feature gives a very blue colour of $F702W - K \lesssim 1.7$. Additionally, there are several other galaxies near this source, some of which are in very close proximity to the host galaxy. Roche, Eales & Rawlings (1998) suggest that this source is currently undergoing a merger with a much smaller galaxy seen to the south east in the *K*-band image, and may be interacting with its other nearby companions, which are also observed in our imaging observations. Roche, Eales & Hippelien (1998) have analysed the clustering properties of most of the galaxies in our $z \sim 1$ 6C subsample. The cross-correlation amplitudes were larger than average for 6C1011+36, consistent with Abell 2 clustering around this source, unlike the Abell class 0 environments found for the majority of the sources in this sample. The line emission from this source does not dominate the aligned emission, and is well explained purely by photoionization by an obscured AGN.

6C1017+37

6C1017+37, at $z = 1.053$, has an elliptical appearance in both the HST and UKIRT images (Fig. 4). Although no radio core is apparent at 5GHz, a faint core was detected by Best et al (1999) in their 8GHz observation. This source is highly asymmetric in the angular sizes of its radio lobes, and its rotation measures. The HST image shows an arc of aligned emission extending into the shorter, north-

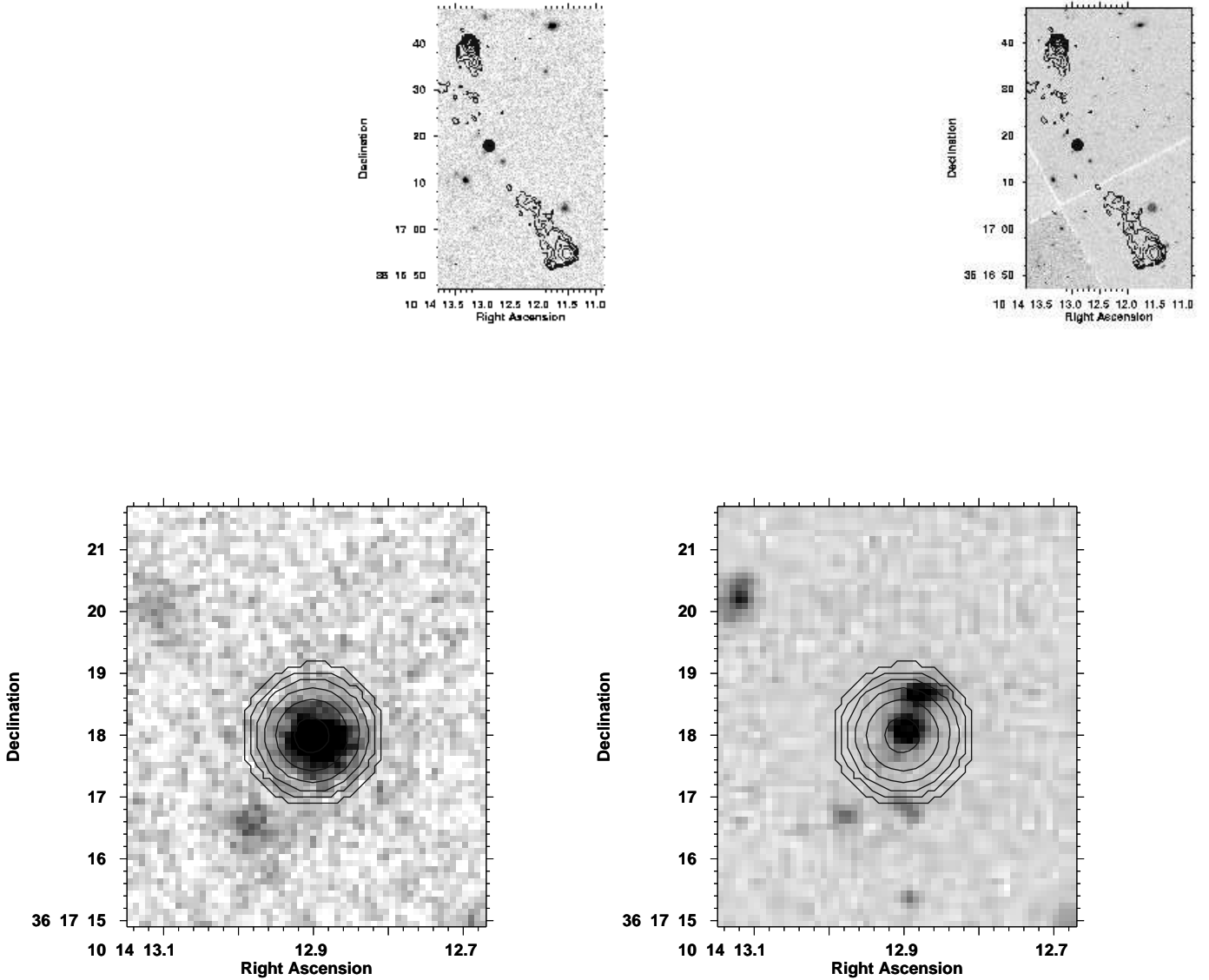


Figure 3. 6C1011+36: (a - top left) K -band image of 6C1011+36. (b - top right) HST F702W image of 6C1011+36. (c - bottom left) zoomed in K -band image of the central region of 6C1011+36. (d - bottom right) zoomed in HST F702W image of the central region of 6C1011+36. Contour lines for all images represent the 5GHz VLA observation of this source, with contours at $80\mu\text{Jy beam}^{-1} \times (-1, 1, 2, 4, \dots, 1024)$. All coordinates are in epoch J2000.0.

eastern radio lobe. The HST emission contains a strong contribution from line emission and nebular continuum emission. Spectroscopic observations of this source show that its emission line region is fairly compact, and displays a very large velocity width ($\sim 900\text{km s}^{-1}$). The spectra are best explained by a mixture of ionization mechanisms: both ionization by radio source shocks and photoionization by an obscured AGN (Inskip et al 2002a). When compared with the data for other radio galaxies at this redshift, the $J - K$ colour obtained from the UKIRT images for this source is particularly blue. In addition to this, the $F702W - K$ colour for this galaxy is the bluest in the 6C subsample.

6C1019+39

6C1019+39, at $z = 0.922$, is the brightest and lowest redshift galaxy in the sample. The combination of the images in the two HST filters (Fig. 5) show that this galaxy is very red in colour, especially when compared to the two other sources observed in more than one HST filter (6C1217+36 and 6C1257+36). The host galaxy appears to be slightly elongated, and no obvious aligned structures can be observed. No radio core has been observed for this source. The position of the host galaxy relative to the radio emission suggests that the radio source is bent, with the radio jets lying on two different axes, the southern jet being directed roughly

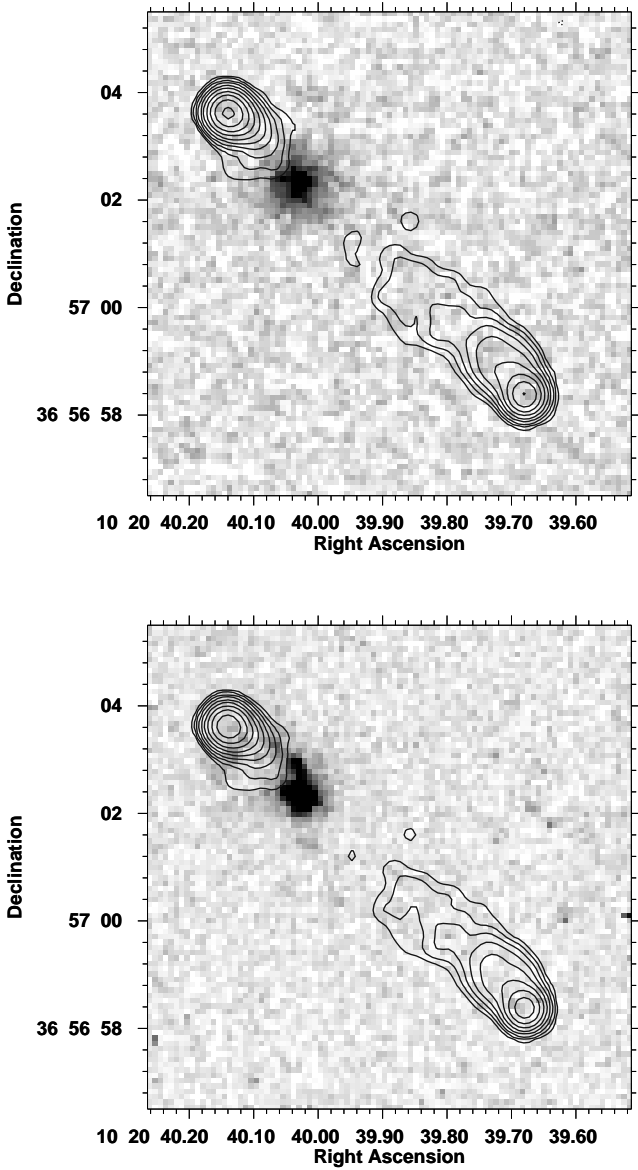


Figure 4. 6C1017+37: (a - top) K -band image of 6C1017+37. (b - bottom) HST F702W image of 6C1017+37. Contour lines for both images represent the 5GHz VLA observation of this source, with contours at $80\mu\text{Jy beam}^{-1} \times (-1,1,2,4\dots 1024)$. All coordinates are in epoch J2000.0.

due south and the northern jet being directed roughly north east. The southern lobe contains an additional hotspot. 6C1019+39 is one of the smaller galaxies in the $z \sim 1$ subsample, with a projected size of 67kpc. The optical (rest-frame UV) spectrum of this source displays a high velocity emission line component, and is well explained with radio source shocks as the dominant ionization mechanism. The high velocity component cannot be clearly linked to any optical structure, and is offset to the north east of the peak of the continuum emission by less than 1 arcsec.

6C1100+35

6C1100+35, at $z = 1.44$, is one of the three higher redshift sources in the sample. Fig. 6 shows that this galaxy does not show any noticeable aligned emission, although it does have a close companion galaxy $\sim 1''$ to the south. The F814W- K colour for 6C1100+35 is

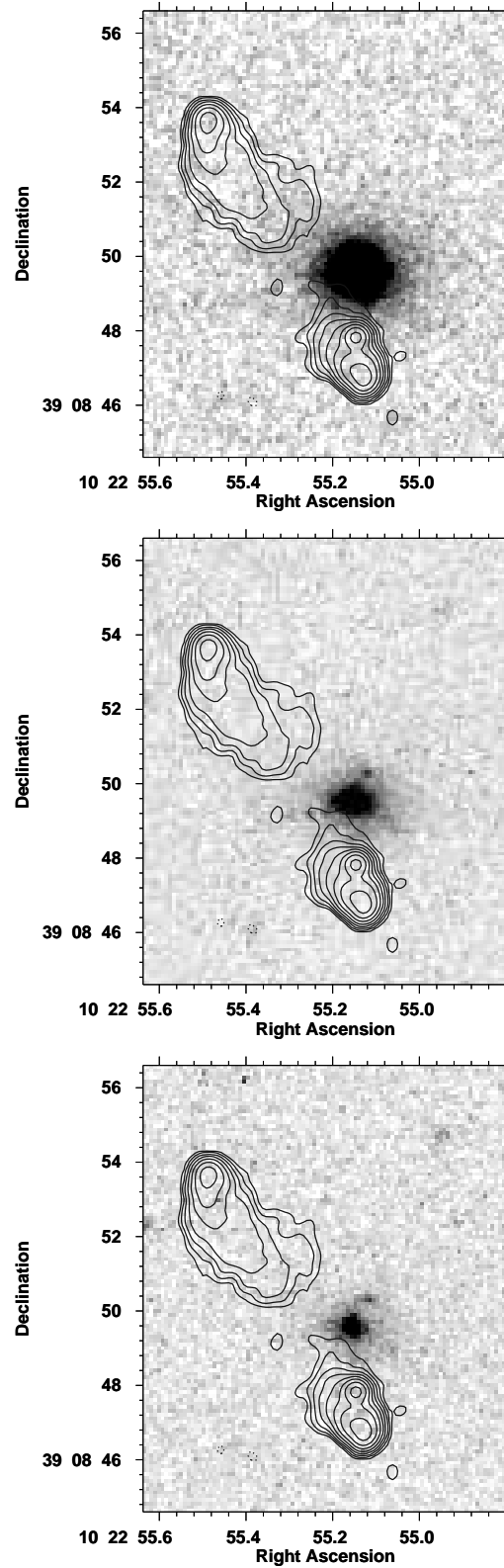


Figure 5. 6C1019+39: (a - top) K -band image of 6C1019+39. (b - centre) HST F814W image of 6C1019+39. (c - bottom) HST F606W image of 6C1019+39. Contour lines for all images represent the 5GHz VLA observation of this source, with contours at $90\mu\text{Jy beam}^{-1} \times (-1,1,2,4\dots 1024)$. All coordinates are in epoch J2000.0.

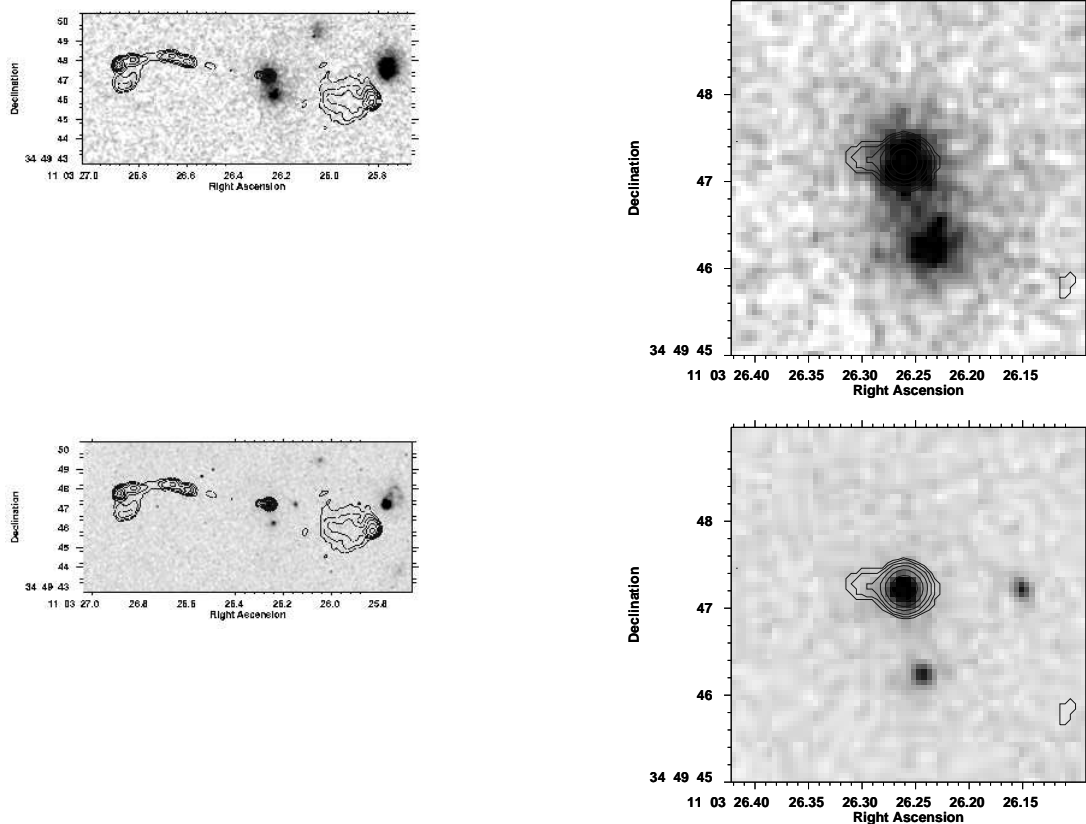


Figure 6. 6C1100+35: (a - top left) K -band image of 6C1100+35. (b - top right) zoomed in K -band image of the central region of 6C1100+35. (c - bottom left) HST F814W image of 6C1100+35. (d - bottom right) zoomed in HST F814W image of the central region of 6C1100+35. Contour lines for all images represent the 5GHz VLA observation of this source, with contours at $100\mu\text{Jy beam}^{-1} \times (-1, 1, 2, 4, \dots, 1024)$. All coordinates are in epoch J2000.0.

redder than average for the sample, but in keeping with the colours of other higher redshift 6C and 3CR sources. The fraction of the total radio flux observed in the bright core is considerably higher than average for the sample. A powerful jet is also observed for this source, and the radio structure of 6C1100+35 is very similar to that of a quasar. However, this source has not been classed as a quasar, due to the lack of any broad lines in its spectrum (Rawlings, Eales & Lacy 2001). The radial profile of the HST emission (see Paper 2 for the full analysis of the radial profiles) suggests a de Vaucouleurs profile, possibly with a very minor contribution from an AGN at small radii. In addition the K -band emission is clearly extended. The average colours of this source support the interpretation that it is a radio galaxy rather than a quasar.

6C1129+37

6C1129+37, at a redshift of $z = 1.060$, is a very interesting radio galaxy. Infrared imaging (Fig. 7) shows two elliptical galaxies of a similar size in close proximity. The radio source jet passes very close to the companion galaxy (W) of the radio source (E). The HST image shows a number of bright knots and extended features surrounding both galaxies, none of which are visible in the infrared images. It is quite likely that these galaxies are interacting with each other. On the HST image, the radio source is identified with the second brightest eastern knot, and the companion galaxy with the brightest western knot. This is illustrated by Fig. 7d, where the UKIRT contours clearly identify the location of the galaxies on the HST image. Although no radio core has been observed for

this source, the galaxy identified with the radio source is coincident with the peak of the line emission, and lies more directly between the two radio lobes. The south eastern lobe contains three hotspots, and is more strongly polarized than the northern radio lobe.

The extensive emission surrounding both galaxies is not dominated by line emission, unlike 6C0943+39. The line emission from this source is most important close to the radio galaxy. The spectra of this source suggest that shock ionization is not an important factor, but AGN photoionization does not predict the line ratios well either, suggesting that a complex combination of ionization mechanisms may be at work. The gas surrounding the radio galaxy displays a very steep velocity gradient, whereas that surrounding the companion galaxy is at a roughly constant relative velocity (Inskip et al 2002a).

The measured $F702W - K$ for this galaxy is very blue, even excluding the bright blue feature to the north which may perhaps be associated with the radio galaxy. This blue colour is due to the extensive aligned emission surrounding both galaxies observed on the HST image. The $J - K$ colour is fairly average for the subsample, however. The companion galaxy is fractionally fainter in K , with a bluer value for $F702W - K$. In places on the HST image, the extended emission is brighter than the radio galaxy it surrounds. The morphology of the excess UV emission surrounding this source is the most extreme observed in the 6C subsample.

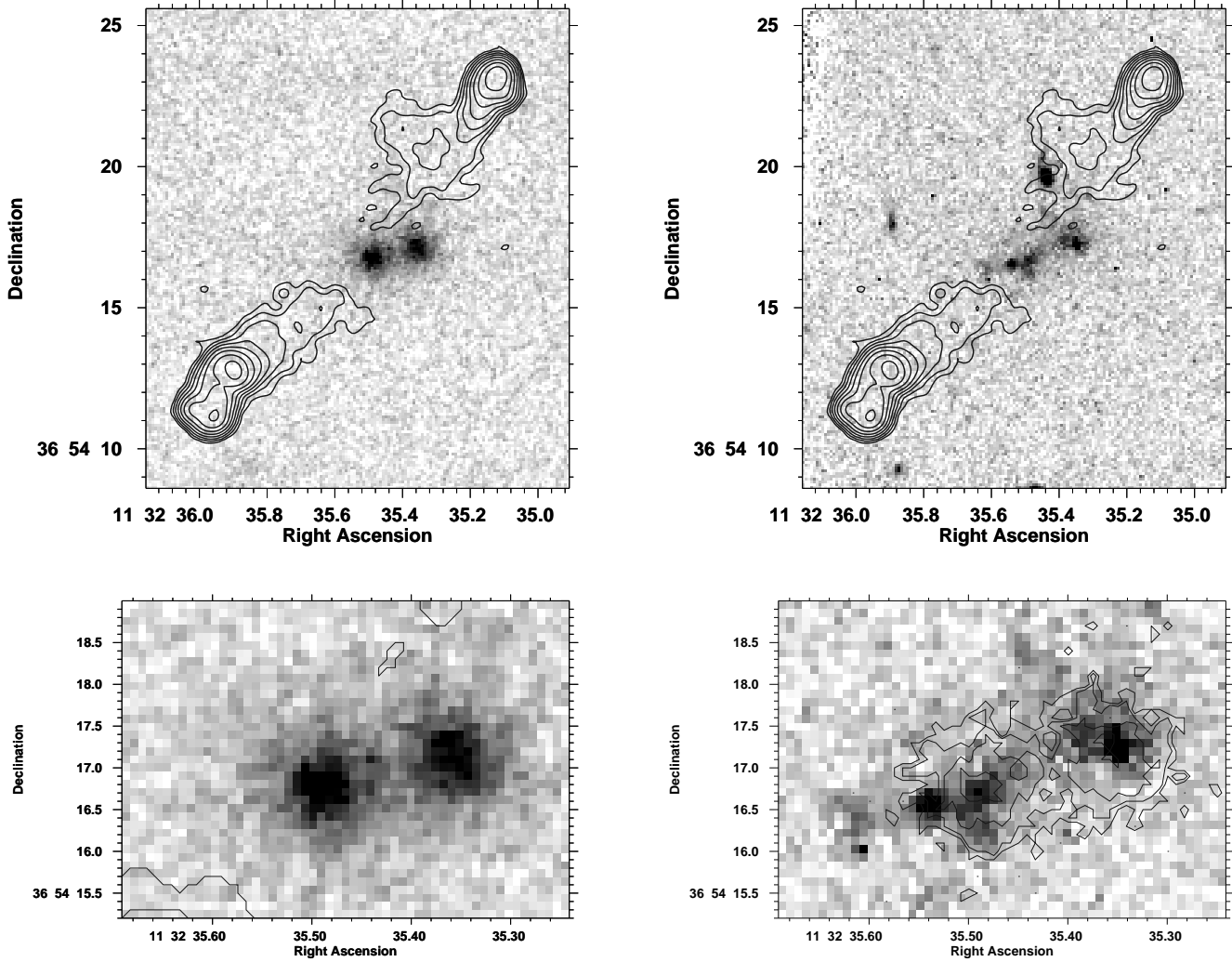


Figure 7. 6C1129+37: (a - top left) K -band image of 6C1129+37, with VLA 5GHz radio contours at $70\mu\text{Jy beam}^{-1} \times (-1, 1, 2, 4, \dots, 1024)$. (b - top right) HST F702W image of 6C1129+37, with VLA 5GHz radio contours. (c - bottom left) zoomed in K -band image of the central region of 6C1129+37, with VLA 5GHz radio contours. (d - bottom right) zoomed in HST F702W image of the central region of 6C1129+37, with UKIRT K -band contours. All coordinates are in epoch J2000.0.

6C1204+35

6C1204+35, at $z = 1.37$, is the third high redshift source in the sample. The colours calculated for this source are average for its redshift. There is some doubt as to the origin of the aligned emission visible on the HST image (Fig. 8), which could perhaps be a tidal arc associated with a faint spiral companion to the north (12 07 32.0 +35 03 10). Alternatively, both the arc and the possible spiral companion could simply be extended emission features related to the AGN activity. Line emission and nebular continuum emission are clearly important contributors to the total emission from this source (cf. Table 3), although new deep spectroscopic observations are not available for this source. Therefore, it is unknown whether AGN photoionization or ionization by shocks is the dominant ionization mechanism.

6C1217+36

6C1217+36 ($z = 1.088$) does not appear to be a standard FRII radio source, and is an anomalous galaxy in the sample. Radio observations show a compact double source in the centre, surrounded by a more extensive halo radio emission. Unusually, the central regions of this source are not depolarized, as would be expected for radio emission from well within the host galaxy. The imaging observations (Fig. 9) simply show a bright elliptical galaxy, with no trace of any aligned emission. However, the radial profile of the HST emission (analysed in full in Paper 2) seems to show evidence for a point source contribution, particularly in the F606W filter. Although this galaxy has a similar F606W-F814W colour to 6C1257+36 (which has also been observed in two HST filters, and is at a similar redshift), the arc of aligned emission present in the images of 6C1257+36 is brightest in the F606W filter, suggesting that of these two sources 6C1217+36 has a bluer host galaxy in this colour. However, the F814W- K colour for this source is fairly red, consistent with that of a passive elliptical galaxy at this red-

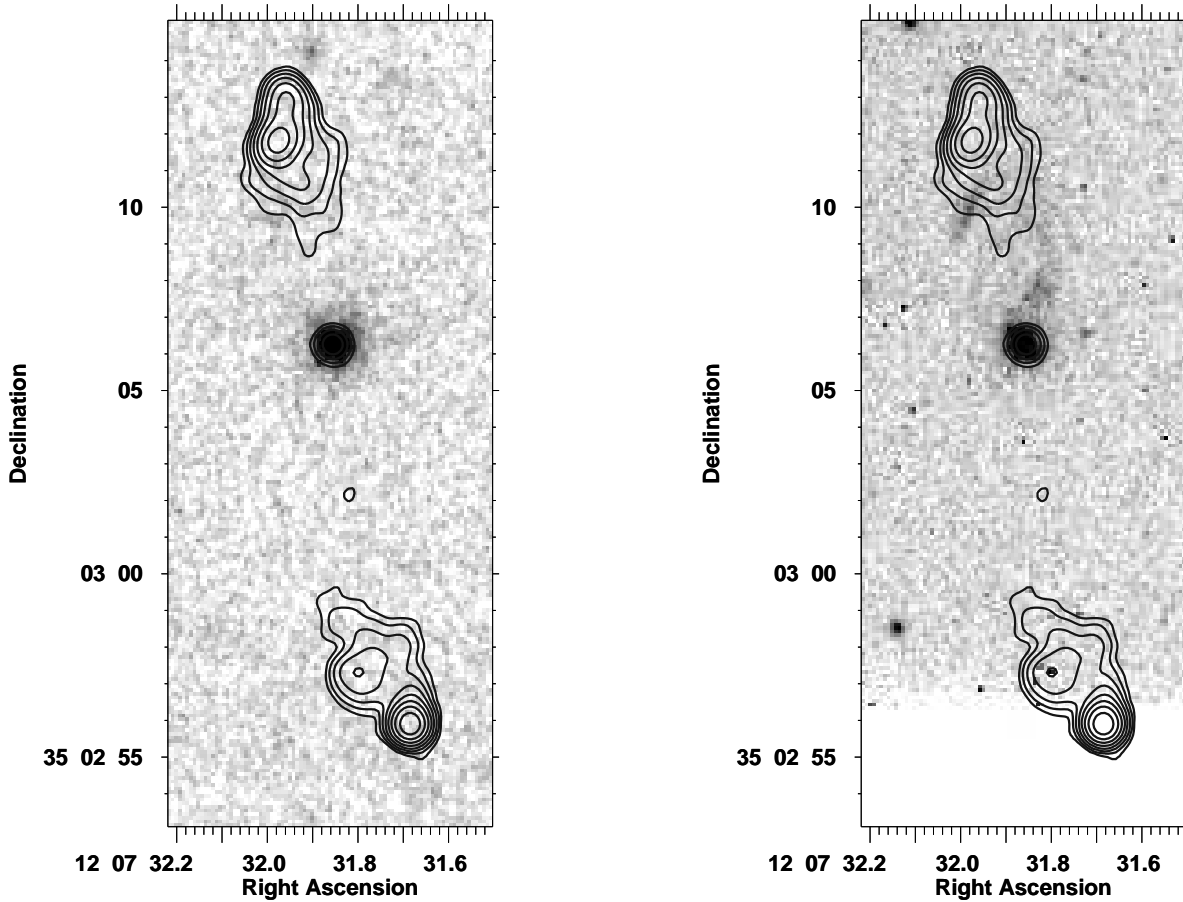


Figure 8. 6C1204+35: (a - left) K -band image of 6C1204+35. (b - right) HST F814W image of 6C1204+35. Contour lines for both images represent the 5GHz VLA observation of this source, with contours at $150\mu\text{Jy beam}^{-1} \times (-1, 1, 2, 4, \dots, 1024)$. All coordinates are in epoch J2000.0.

shift. Deep spectroscopic observations show that this source has very weak line emission.

6C1256+36

The UKIRT images of 6C1256+36 ($z = 1.128$) show a seemingly elongated elliptical galaxy (Fig. 10). With UKIRT K -band contours overlaid on the HST F702W image, it is seen that the brightest component of the HST emission does not lie at the peak of the K -band emission. The K -band image is also extended in this region. The combined HST and UKIRT observations of this source show that this extended emission region is bluer than the elliptical host galaxy of the radio source, and is most likely due to the alignment effect. Roche, Eales & Hippelein (1998) found that 6C1256+36 exists in a richer environment than average for radio galaxies at $z \sim 1$, and claim that it lies within an Abell class 2 cluster. The $J - K$ and $F702W - K$ colours for this source are average for the sample. Spectroscopic observations of this source suggest that both shock ionization and AGN photoionization are important. No radio core has been observed for this source.

6C1257+36

The radio contours for 6C1257+36 ($z = 1.004$) show two possible core candidates, of which the NW knot has been found to be coincident with the host galaxy (Fig. 11). Best *et al* (1999) correctly identified the fainter, NW knot as the radio core due to its flatter spectral index. In addition, the south eastern lobe displays a double hotspot and little polarized emission. The HST imaging of 6C1257+36 in two filters shows that this radio galaxy has a fairly red elliptical host galaxy, consistent with an old stellar population, with a blue arc of aligned emission. The blue arc appears to be nearly coincident with the SE knot in the radio emission. A further small region of bluer emission is observed to the northwest, again aligned with the radio axis.

The spectra of this source show that the line emission is well explained by photoionization by an obscured AGN. However, the large physical extent of the line emission and its extreme kinematic properties suggest that the line emitting regions in this source have been influenced by the radio knot, which may have recently passed through the gas clouds forming the arc. The F814W – F606W colour for this galaxy is comparable to that of 6C1217+36, and considerably bluer than that of 6C1019+39. However, this source displays extensive blue aligned emission whereas 6C1217+36 does not. Nebular continuum emission is significant in

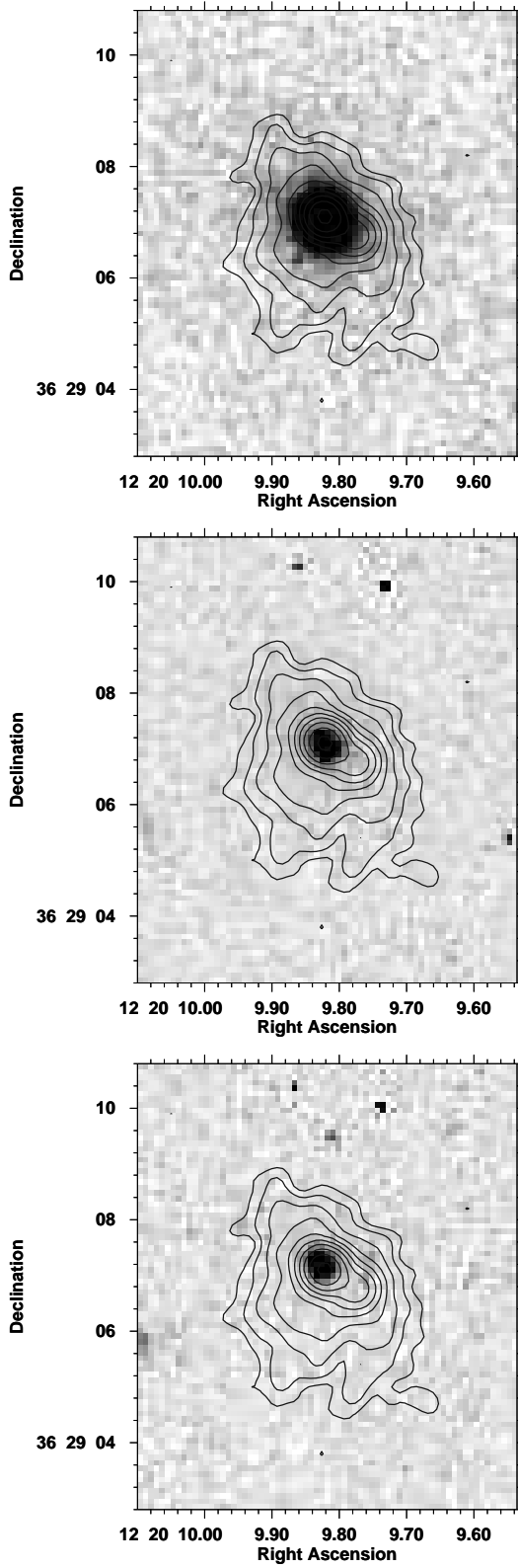


Figure 9. 6C1217+36: (a - top) K -band image of 6C1217+36. (b - centre) HST F814W image of 6C1217+36. (d - bottom) HST F606W image of 6C1217+36. Contour lines for all images represent the 5GHz VLA observation of this source, with contours at $150\mu\text{Jy beam}^{-1} \times (-1, 1, 2, 4 \dots 1024)$. All coordinates are in epoch J2000.0.

both filters whereas line emission is only significant in the redder of the two filters; the blue arc is clearly an important continuum emission feature associated with an alternative emission mechanism.

5 DISCUSSION

The initial results of the imaging observations and a preliminary analysis of the galaxy colours have provided a number of interesting results. By combining the results of the imaging observations with previous deep spectroscopic observations (Inskip et al 2002a) we have been able to determine the contribution of several different emission mechanisms to the aligned emission. Line emission and nebular continuum emission are present in the wavelength range sampled by the HST observations, in similar proportions to that found in observations of 3CR sources at the same redshift. Whilst these processes are important in the diffuse extended emission surrounding 6C0943+39 (contributing up to 50% of the observed flux at a distance of $>4''$ from the host galaxy), the bright, blue knotty features observed around 6C1129+37 cannot be explained by regions of bright line emission. Overall, line emission and nebular continuum emission are not the dominant processes producing the alignment effect in these galaxies.

In general, the magnitudes determined within the $4''$ and $9''$ diameter apertures are comparable. Any differences can be fully accounted for by the presence of very extended UV/optical emission (e.g. 6C1129+37, 6C1204+35) and the extended nature of the host galaxies, which typically have characteristic radii of $\sim 1\text{-}3''$ (Best et al 1998; subsequent papers in this series (in prep)). For several sources, the galaxy colours are complicated by the presence of point source contributions from the AGN. An accurate quantification of the point source contributions and detailed analysis of the galaxy colours, including a comparison with 3CR sources in order to investigate the influence of radio power, has therefore been deferred to a later paper in this series. Although a full morphological analysis of the galaxies is also deferred to a later paper, several conclusions can be reached simply on the basis of the observed appearance of the galaxies.

- The infrared observations of the $z \sim 1$ 6C radio galaxies do not display any significant extended emission aligned along the radio axis. A similar result was obtained for the K band observations of 3CR sources at the same redshift, confirming the wavelength dependence of the alignment effect. The slightly more elongated appearance of the galaxy 6C1256+36 is most likely to indicate an elongated elliptical morphology, rather than extended aligned emission in the K -band or alternatively the presence of a close companion galaxy.

- A number of sources appear to be interacting or undergoing mergers. These include 6C1011+36, previously proposed to be associated with a rich Abell class 2 cluster (Roche, Eales & Hippelein 1998). 6C1129+37 is clearly shown to be two merging ellipticals, rather than a single galaxy with bright aligned infrared emission, as had previously been considered. 6C1100+35 appears to have a close companion to the south.

- A wide range of extended structures are observed in the HST images of the 6C galaxies. Some sources show considerable extended emission, which is generally well aligned with the radio source axis. The variety of features observed are generally very similar to those seen around 3CR sources at the same redshift, and include bright knots, diffuse emission, linear features and arcs. In particular, arc-like aligned structures are observed around 6C1017+37 and 6C1204+35, reminiscent of those seen around

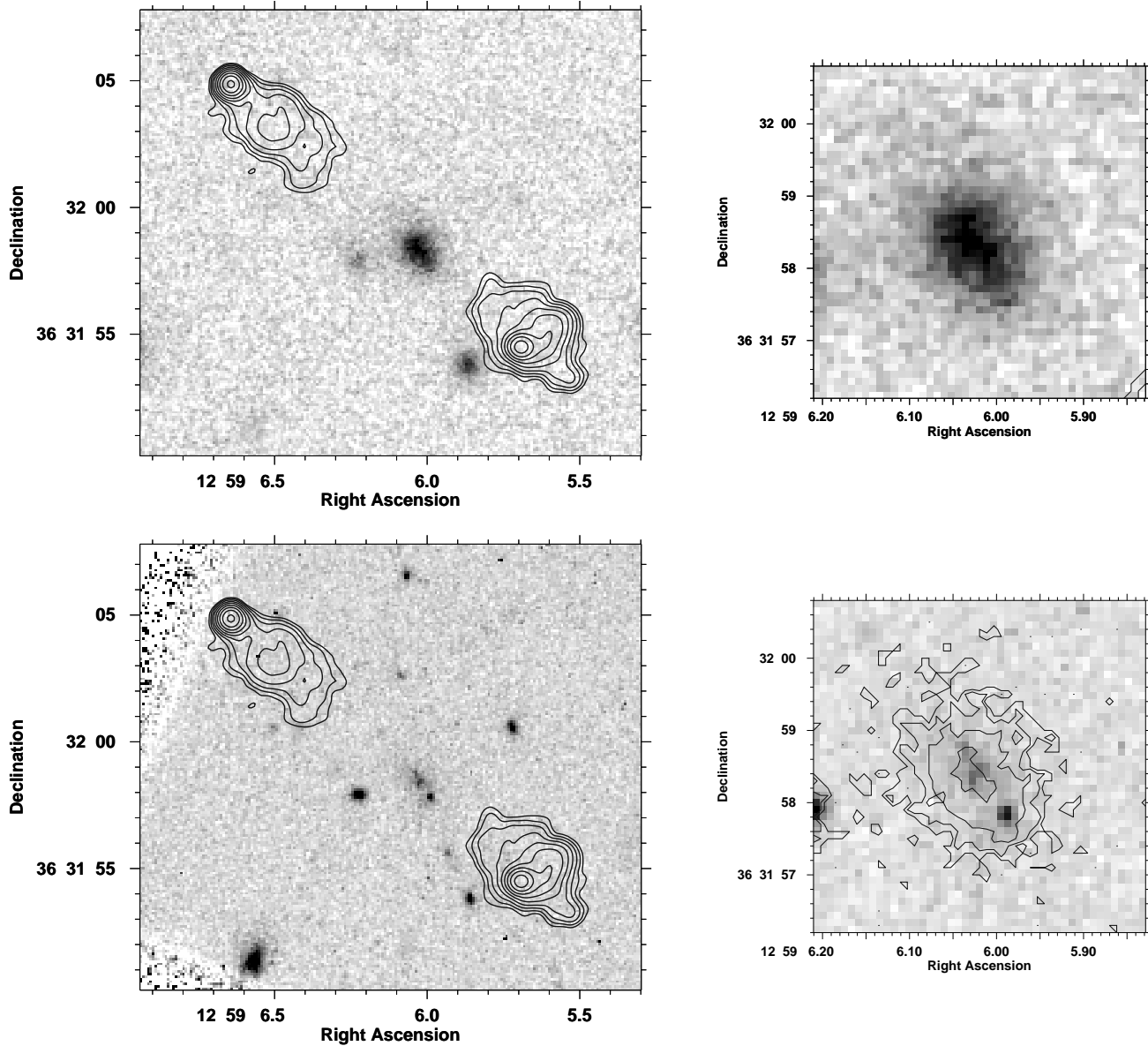


Figure 10. 6C1256+36: (a - top left) K -band image of 6C1256+36, with VLA 5GHz radio contours at $100\mu\text{Jy beam}^{-1} \times (-1, 1, 2, 4, \dots, 1024)$. (b - bottom left) HST F702W image of 6C1256+36, with VLA 5GHz radio contours. (c - top right) zoomed in K -band image of the central region of 6C1256+36. (d - bottom right) zoomed in HST F702W image of the central region of 6C1256+36, with UKIRT K -band contours. All coordinates are in epoch J2000.0.

3C280 and 3C267. Optically passive sources are also found in both samples (e.g. 6C1019+39, 6C1217+36 and 3C65). However there are some features, such as the bright blue object to the north of 6C1129+37, which (if indeed associated with AGN activity) do not resemble anything previously observed in the more powerful 3CR subsample.

- As in the case of the 3CR $z \sim 1$ subsample, extreme features were typically not observed around the larger radio galaxies in the sample. However, the strong trend observed in the 3CR subsample for the smaller sources to display several bright knots of aligned emission is not seen in the 6C data. On the whole, the aligned features observed around the 6C sources appear less luminous and less extensive than those surrounding $z \sim 1$ 3CR radio sources. Fewer bright emission components are observed, and these are generally situated in closer proximity to the host galaxy.

ACKNOWLEDGEMENTS

KJI acknowledges the support of a PPARC research studentship and a Lloyds Tercenary Foundation Research Fellowship. PNB is grateful for the generous support offered by a Royal Society Research Fellowship. The United Kingdom Infrared Telescope is operated by the Joint Astronomy Centre on behalf of the U.K. Particle Physics and Astronomy Research Council. Some of the data reported here were obtained as part of the UKIRT Service Programme. Parts of this research are based on observations made with the NASA/ESA Hubble Space Telescope, obtained at the Space Telescope Science Institute, which is operated by the Association of Universities for Research in Astronomy, Inc., under NASA contract NAS 5-26555. These observations are associated with proposals #6684 and #8173.

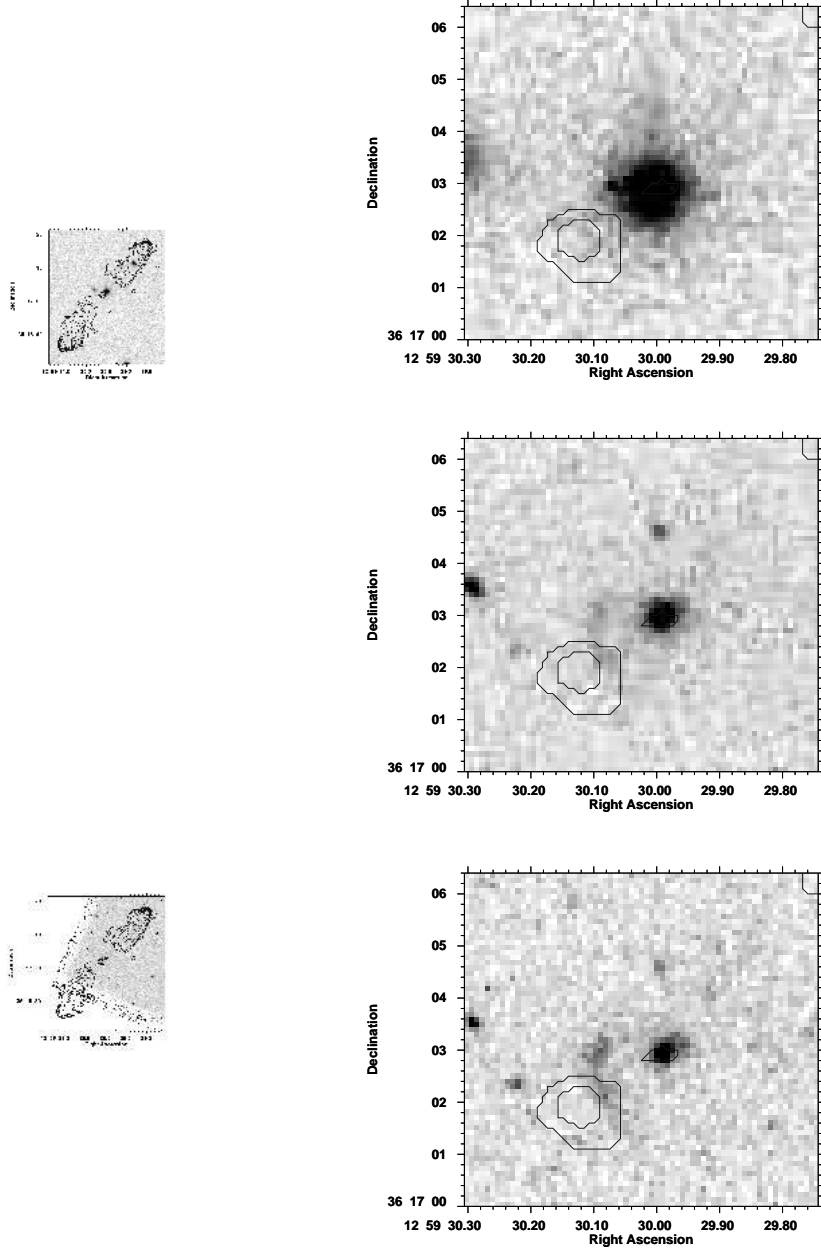


Figure 11. 6C1257+36: (a - top left) K -band image of 6C1257+36. (b - bottom left) HST F606W image of 6C1257+36. (c - top right) zoomed in K -band image of 6C1257+36. (d - centre right) zoomed in HST F814W image of 6C1257+36. (e - bottom right) zoomed in HST F606W image of 6C1257+36. Contour lines for all images represent the 5GHz VLA observation of this source, with contours at $80\mu\text{Jy beam}^{-1} \times (-1, 1, 2, 4, \dots, 1024)$. All coordinates are in epoch J2000.0.

REFERENCES

Aller L., 1987, *Astrophys. Space Sci. Library* Vol. 112, Physics of Thermal Gaseous Nebulae. Reidel, Dordrecht

Best P. N., Longair M. S., Röttgering H. J. A., 1997, *MNRAS*, 292, 758

Best P. N., Longair M. S., Röttgering H. J. A., 1998, *MNRAS*, 295, 549

Best P. N., Eales S. A., Longair M. S., Rawlings S., Röttgering H. J. A., 1999, *MNRAS*, 303, 616

Best P. N., Röttgering H. J. A., Longair M. S., 2000, *MNRAS*, 311, 1

Bicknell G. V., Sutherland R. S., van Breugel W. J. M., Dopita M. A., Dey A., Miley G. K., 2000, *ApJ*, 540, 678

Biretta, Lubin et al, 2002, WFPC2 Instrument Handbook, Version 7.0 (Baltimore: STScI)

Blundell K. M., Rawlings S., Willott C. J., 1999, *ApJ*, 117, 677

Bremer M. N., Fabian A. C., Crawford C. S., 1997, *MNRAS*, 284, 213

Chambers K. C., Miley G. K., van Breugel W. J. M., 1987, *Nature*, 329, 604

Clark N. E., Axon D. J., Tadhunter C. N., Robinson A., O'Brien P., 1998, *ApJ*, 494, 546

Cimatti A., di Serego Alighieri S., Fosbury R. A. E., Salvati M., Taylor D., 1993, *MNRAS*, 264, 421

Dey A., van Breugel W., Vacca W. D., Antonucci R., 1997, *ApJ*, 490, 698

Dickson R., Tadhunter C., Shaw M., Clark N., Morganti R., 1995, *MNRAS*, 273, L29

Dolphin A. E., 2000, PASP, 112, 1397

Eales S. A., 1985, MNRAS, 217, 149

Eales S. A., Rawlings S., Law-Green D., Cotter G., Lacy M., 1997, MNRAS, 291, 593

Holtzman J. A., Burrows C. J., Casertano S., Hester J. J., Trauger J. T., Watson A. M., Worthey G., 1995, PASP, 107, 1065

Howarth I. D., 1983, MNRAS, 203, 301

Inskip K. J., Best P. N., Rawlings S., Longair M. S., Cotter G., Röttgering H. J. A., Eales S. A., 2002a, MNRAS, 337, 1381

Inskip K. J., Best P. N., Röttgering H. J. A., Rawlings S., Cotter G., Longair M. S., 2002b, MNRAS, 337, 1407

Jarvis M. J. *et al.*, 2001, MNRAS, 326, 1563

Kaiser C. R., Dennet-Thorpe J., Alexander P., 1997, MNRAS, 292, 723

Lilly S. J., Longair M. S., Allington-Smith J. R., 1985, MNRAS, 215, 37

Maddox S. J., Efstathiou G., Sutherland W. J., Loveday J., 1990, MNRAS, 243, 692

McCarthy P. J., Spinrad H., van Breugel W. J. M., 1995, ApJS, 99, 27

McCarthy P. J., van Breugel W. J. M., Spinrad H., Djorgovski S., 1987, ApJ., 321, L29

Mellema G., Kurk J. D., Röttgering H. J. A., 2002, A&A, 395, L13

Neeser M. J., Eales S. A., Law-Green J. D., Leahy J. P., Rawlings S., 1995, ApJ, 451, 76

Rawlings S., Eales S., Lacy M., 2001, MNRAS, 322, 523

Rigler M. A., Lilly S. J., Stockton A., Hammer F., Le Fèvre O., 1992, ApJ, 385, 61

Roche N., Eales S. A., Hippelein H., 1998, MNRAS, 295, 946

Roche N., Eales S. A., Rawlings S., 1998, MNRAS, 297, 405

Solórzano-Íñarrea C., Tadhunter C. N., Axon D. J., 2001, MNRAS, 323, 965

Spinrad H. *et al.*, 1997, ApJ, 484, 581

Tadhunter C. N., Scarrott S. M., Draper P., Rolph C., 1992, MNRAS, 256, 53

Tadhunter C. N. *et al.*, 2002, MNRAS, 330, 977

Wardle J. F. C., Miley G. K., 1974, A&A, 30, 305